# Nuclear excitation and control induced by intense vortex lasers

Zhi-Wei Lu,[1,*] Hanxu Zhang,[2,*] Tao Li,[2] Mamutjan Ababekri,[1] Xu Wang,[2,3,†] and Jian-Xing Li[1,4,‡]

[1]*Ministry of Education Key Laboratory for Nonequilibrium Synthesis and Modulation of Condensed Matter, State Key Laboratory of Electrical Insulation and Power Equipment, Shaanxi Province Key Laboratory of Quantum Information and Quantum Optoelectronic Devices, School of Physics, Xi'an Jiaotong University, Xi'an 710049, China*

[2]*Graduate School, China Academy of Engineering Physics, Beijing 100193, China*

[3]*Southern Center for Nuclear-Science Theory, Institute of Modern Physics, Chinese Academy of Sciences, Huizhou, Guangdong 516000, China*

[4]*Department of Nuclear Physics, China Institute of Atomic Energy, P.O. Box 275(7), Beijing 102413, China*

(Received 17 March 2025; revised 11 January 2026; accepted 30 March 2026; published 20 April 2026)

The existing intense laser-based approaches for nuclear excitation offer ultrafast temporal resolution and high efficiency compared to traditional accelerator probes. However, controlling nuclear properties, such as spin and magnetic moment, remains an unprecedented challenge. Here, we put forward a novel method for nuclear excitation and control induced by intense vortex laser. We develop the calculation method incorporating the orbital angular momentum (OAM) of vortex laser within the nuclear hyperfine mixing framework. We find that intense vortex laser can effectively excite hydrogen-like thorium-229 nucleus and induce three-dimensional rotation of the nuclear magnetic moment. This rotation arises from the localized electromagnetic field reconfiguring the population dynamics, and can be reconstructed through radiation spectrum analysis. Moreover, the OAM of vortex laser enables the chaotic system to exhibit topologically protected periodic patterns in nuclear excitation and radiation, facilitating precise experimental measurements. Our findings underscore the potential of vortex laser for high-precision nuclear control and imaging, deepening our understanding of nuclear properties and hyperfine structures, and advancing quantum information and nuclear technologies.

DOI: 10.1103/6m8k-9pcb

## I. INTRODUCTION

Efficient excitation and control of nuclei have long been pursued in nuclear physics, significantly impacting various applications, including quantum information (enhancing qubit coherence) [1,2], medical imaging (improving magnetic resonance imaging resolution) [3–5], materials science (developing novel magnetic materials) [6,7], and fundamental physics (investigating nuclear structure and interactions) [8–13]. Traditional probes for nuclear excitation and control primarily include nuclear magnetic resonance probes that combine external magnetic fields and radiofrequency pulses [5], as well as relativistic (∼MeV) particle beams from accelerators, such as $\gamma$ rays [14], electrons [15], neutrons [16], and ions [17]. The former are mainly suitable for light nuclei with a spin angular momentum of 1/2 with transition energies typically in the microelectronvolt ($\mu$eV) range, limiting their effectiveness for higher-energy transitions and heavy nuclei. The latter is constrained by the limited luminosity of the accelerator beam, which restricts time resolution and excitation efficiency. The rapid development of ultraintense, ultrashort laser facilities has achieved peak intensities of approximately $10^{23}\,\mathrm{W/cm^2}$ with pulse durations in the tens of femtoseconds [18–20]. This progress has catalyzed the development of laser-based proposals for nuclear excitation, encompassing both experimental [21–24] and theoretical [25–27] methodologies that exhibit ultrafast time resolution and ultrahigh excitation efficiency. Nevertheless, the excitation cross sections associated with these approaches remain relatively small. Very recently, research [28] predicts that the highly nonlinear interaction between intense lasers and hydrogenlike thorium-229 ions ($^{229}Th^{89+}$) can excite over 10% of these ions into the isomeric state with a single femtosecond laser pulse, accompanied by high-order harmonic emission. In this scenario, with one electron outside the nucleus, the strong electromagnetic field generated by electrons near the nucleus induces nuclear hyperfine mixing (NHM) among states with the same total angular momentum, substantially shortening the isomeric lifetime by several orders of magnitude and causing slight shifts in hyperfine energy levels [29–32]. Unfortunately, this highly nonlinear interaction renders the excitation and radiation patterns of the system chaotic and unpredictable, limiting control over the nucleus. Overall, current researches are still focused on effectively exciting nuclei, and controlling properties such as nuclear spin and nuclear magnetic moment presents unprecedented challenges.

*These authors contributed equally to this work.
†Contact author: xwang@gscaep.ac.cn
‡Contact author: jianxing@xjtu.edu.cn

 

Meanwhile, recent advancements in the fabrication of phase masks with nanometer precision has rendered it possible to control the coherent superposition of matter waves, which produces typical interference patterns through spatial wave function reshaping [33–36]. Particularly interesting are vortex photons, described by wave functions with helical phases that carry intrinsic orbital angular momentum (OAM) along their propagation axis [37,38]. Currently, vortex photons ranging from visible to x ray (eV∼keV) have been experimentally generated via optical mode conversion, high harmonic techniques, and coherent radiation in helical undulators and contemporary laser facilities [39–43]. Vortex photons, arising from the new degree of freedom, provide unique advantages in optical manipulation, quantum information, and imaging techniques [39,44], which have been predicted and demonstrated in atomic [45–49], molecular [50,51], and larger scales systems [52,53]. The interaction of nuclei with vortex states has garnered attention, with theoretical investigations including multipolar nuclear transitions [54], nuclear clock transitions [55], Δ baryon photoproduction [56], and deuteron photodisintegration [57]. Our previous theoretical studies on relativistic vortex particles, such as $\gamma$ rays [58] and electrons [59], interacting with nuclei in the giant resonance regime (tens of MeV), indicate that vortex particles have the potential to manipulate nuclear transitions and provide new insights into nuclear structure. These findings motivate our ongoing exploration of the interactions between contemporary intense vortex lasers and nuclei exhibiting the NHM effect, which raises questions about the phenomena of nuclear excitation and radiation that may emerge, as well as whether vortex lasers can be utilized for nuclear control.

In this work, we put forward a novel method for nuclear excitation and control using intense vortex laser. We develop a theory incorporating the OAM of vortex laser within the NHM framework. We find that intense vortex laser induces two interesting phenomena in nuclear control Fig. 1(a). (1) Nuclear magnetic moment rotation: The reconfiguration of the system population by the localized electromagnetic field results in a three-dimensional rotation of the nuclear magnetic moment. The radiation spectra retain signatures of this rotational effect, enabling the microscopic rotation reconstruction Fig. 1(b), which enhances our understanding of fundamental nuclear properties (e.g., magnetic susceptibility and spin dynamics) and nuclear structures (e.g., hyperfine energy level structures and populations). (2) Periodic radiation enhancement: When the light-nucleus interaction deviates from the linear perturbation regime, we observe periodic enhancements in the radiation spectra at various azimuthal angles determined by the OAM of vortex laser. The peak values of radiation spectra can be significantly amplified by several orders of magnitude compared to that in nonvortex case. Correspondingly, the isomeric excitation probability, while exhibiting some randomness, also displays a periodic pattern. This indicates that introducing OAM into an otherwise chaotic system leads to the emergence of topologically protected features, presenting ordered and regular patterns that facilitate experimental measurement. Additionally, position-dependence offers a new dimension for precise nuclear state control.

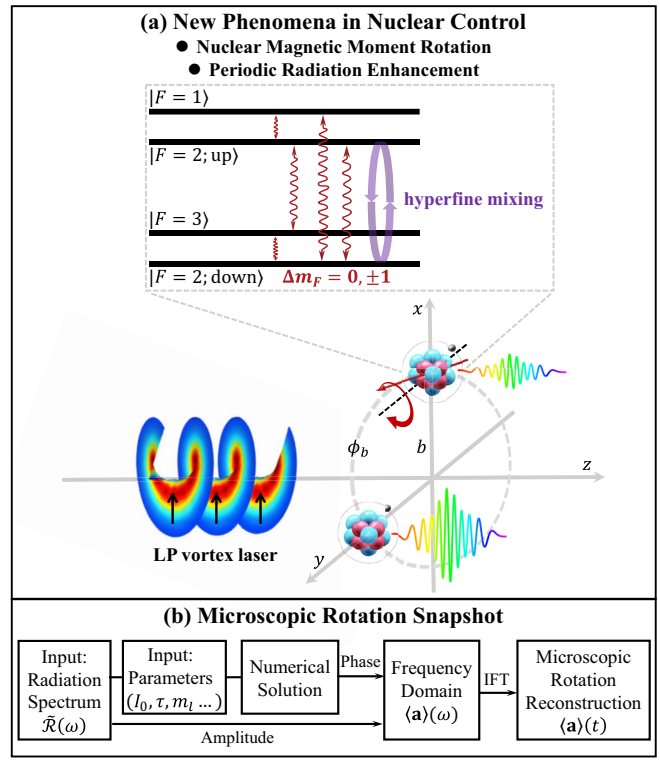


FIG. 1. Interaction scenario between an intense vortex laser and the $^{229}Th^{89+}$ ion. A linearly polarized (LP) vortex laser in the $x$-direction (black arrow) propagates along the $z$-axis. The ion's position relative to the vortex laser's central axis is defined by the impact parameter **b**, comprising distance $b$ and azimuthal angle $\phi_b$. State mixing of the two levels with total angular momentum $F = 2$ arises from the NHM effect. The transition selection rules for changes in the magnetic quantum number $\Delta m_F$ are modified from the previous $\pm 1$ to $0, \pm 1$. (a) New Phenomena in Nuclear Control: Vortex laser-induced high-order harmonic radiation (rainbow-colored pulses) exhibits periodic enhancement at various azimuthal angles $\phi_b$, with the period determined by OAM projection $m_l$. The average acceleration $\langle \mathbf{a} \rangle$ of the nuclear magnetic moment rotates during radiation (red arrow). (b) Microscopic Rotation Snapshot: The radiation spectrum $\tilde{\mathcal{R}}(\omega)$, combined with theoretical calculations, reconstructs the acceleration's frequency-domain signal. Here $\omega$, $I_0$ and $\tau$ denote radiation frequency, laser peak intensity, and pulse duration, respectively. Inverse Fourier transform (IFT) yields the time-domain rotational signal.

The paper is organized as follows. Section II introduces the theoretical framework. Section III presents: (1) nuclear magnetic moment rotation, (2) topologically protected periodic patterns, and (3) experimental feasibility. Section IV provides a brief conclusion.

## II. THEORETICAL FRAMEWORK

Traditional photonuclear interaction theory [28,60–62] does not directly apply to vortex light carrying OAM. Recent advances in vortex light-nucleus interaction [55,58] primarily focus on weak-intensity, resonant-absorption regime while neglecting the NHM effects. Here, we consider the interaction

between the $^{229}Th^{89+}$ ion and an intense vortex laser pulse with a wavelength of 800 nm. The ion is initially in its ground state $|F=2;\text{down}\rangle$. The Hamiltonian for the $^{229}Th^{89+}$ ion is defined as $H_0 = H_e + H_n + V_{HF}$, where $V_{HF}$ represents the hyperfine interaction [63,64], causing minor adjustments in the energies of hyperfine levels and state mixing between two $F=2$ levels, with the NHM coefficient $c_m \approx -0.031$ in our calculations [61]. The evolution of the four-level system ($|F=2;\text{down}\rangle$, $|F=3\rangle$, $|F=2;\text{up}\rangle$, $|F=1\rangle$) is determined by the time-dependent Schrödinger equation [65]

$$i\hbar\frac{\partial}{\partial t}|\Psi(t)\rangle = \left[H_0(t) + H_I^V(t)\right]|\Psi(t)\rangle, \tag{1}$$

where the interaction Hamiltonian with the vortex laser $H_I^V(t)$ incorporates contributions from the current density operators of the electron and nucleus [63,66]: $H_I^V(t) = -\frac{1}{c}\int[\boldsymbol{j}_e(\boldsymbol{r}) + \boldsymbol{j}_n(\boldsymbol{r})]\cdot\boldsymbol{A}^V(\boldsymbol{r},t)d\boldsymbol{r}$. The vector potential of vortex laser $\boldsymbol{A}^V$ is exemplified by the Bessel-Gauss mode [67] and assumed to be LP in the $x$ direction under the paraxial approximation. Experiments typically focus on paraxial light beams, where the transverse photon momentum is much smaller than its longitudinal counterpart, i.e., $\varkappa = |\boldsymbol{k}_\perp| \ll k_z$, such that OAM projection $m_l$ becomes decoupled from helicity $\Lambda$. The LP vector potential can be composed of two circular polarization components [68]

$$\boldsymbol{A}^V = \frac{i}{\sqrt{2}}\left(\boldsymbol{A}^{BG}_{m_\gamma=m_l+1,\Lambda=1} - \boldsymbol{A}^{BG}_{m_\gamma=m_l-1,\Lambda=-1}\right), \tag{2}$$

where $m_\gamma$ is the projection of total photon angular momentum along the propagation direction. In momentum space, the vector potential $\boldsymbol{A}^{BG}_{\varkappa k_z m_\gamma\Lambda}$ can be expressed as a coherent superposition of plane waves,

$$\boldsymbol{A}^{BG}_{\varkappa k_z m_\gamma\Lambda}(\boldsymbol{r}) = \int\frac{d^2\boldsymbol{k}_\perp}{(2\pi)^2}a^{BG}_{\varkappa m_\gamma}\hat{e}_\nu e^{i\boldsymbol{k}\cdot\boldsymbol{r}}, \tag{3}$$

where $\hat{e}_\nu$ is a spherical unit vector with $\hat{e}_0 = \hat{z}$ and $\hat{e}_{\pm1} = \frac{1}{\sqrt{2}}(\hat{x}\pm i\hat{y})$. The corresponding Fourier amplitude is given by

$$a^{BG}_{\varkappa m_\gamma} = \pi i^{m_\gamma}e^{im_\gamma\phi_k}w_0^2\exp\left[-\frac{\varkappa^2+k_\perp^2}{4}w_0^2\right]I_{m_\gamma}\left(\frac{\varkappa w_0^2}{2}k_\perp\right), \tag{4}$$

where $\phi_k$, $w_0$ and $I_{m_\gamma}$ denote the azimuthal angle of $\boldsymbol{k}_\perp$, the beam waist and the modified Bessel function, respectively.

When $w_0$ is sufficiently large compared to other relevant length scales (e.g., the wavelength), the modified Bessel function can be approximated by its asymptotic form, allowing one to evaluate the integral explicitly. In that limit, the time-independent interaction matrix element can be expressed as

$$\begin{aligned}
&\langle F=3|E_I^V|F=2;\text{down}\rangle\\
&= (-1)^{m_{F_i}}\mathcal{E}_0\begin{pmatrix}2 & 1 & 3\\ m_{F_i} & \Delta m_F & -m_{F_f}\end{pmatrix}\left[\sqrt{1-c_m^2}\left(\sqrt{\frac{7}{30}}\mu_{gs} - \sqrt{\frac{35}{6}}\mu_e\right) + c_m\frac{2\sqrt{7\pi}}{3}\sqrt{B(M1)}\right]\\
&\quad\times(-i)^{2m_l-\Delta m_F+2}e^{-b^2/w_0^2}\left[e^{i(m_l+1-\Delta m_F)\phi_b}d^1_{\Delta m_F 1}(\theta_k)J_{m_l+1-\Delta m_F}(\varkappa b) - e^{i(m_l-1-\Delta m_F)\phi_b}d^1_{\Delta m_F-1}(\theta_k)J_{m_l-1-\Delta m_F}(\varkappa b)\right], \quad (5a)\\
&\langle F=1|E_I^V|F=2;\text{down}\rangle\\
&= (-1)^{m_{F_i}}\mathcal{E}_0\begin{pmatrix}2 & 1 & 1\\ m_{F_i} & \Delta m_F & -m_{F_f}\end{pmatrix}\left[\sqrt{1-c_m^2}\sqrt{2\pi}\sqrt{B(M1)} + c_m\left(\frac{\sqrt{5}}{2\sqrt{3}}\mu_{is} - \frac{\sqrt{15}}{2}\mu_e\right)\right]\\
&\quad\times(-i)^{2m_l-\Delta m_F+2}e^{-b^2/w_0^2}\left[e^{i(m_l+1-\Delta m_F)\phi_b}d^1_{\Delta m_F 1}(\theta_k)J_{m_l+1-\Delta m_F}(\varkappa b) - e^{i(m_l-1-\Delta m_F)\phi_b}d^1_{\Delta m_F-1}(\theta_k)J_{m_l-1-\Delta m_F}(\varkappa b)\right], \quad (5b)\\
&\langle F=2;\text{up}|E_I^V|F=3\rangle\\
&= (-1)^{m_{F_i}}\mathcal{E}_0\begin{pmatrix}3 & 1 & 2\\ m_{F_i} & \Delta m_F & -m_{F_f}\end{pmatrix}\left[\sqrt{1-c_m^2}\frac{-2\sqrt{7\pi}}{3}\sqrt{B(M1)} + c_m\left(\sqrt{\frac{7}{30}}\mu_{gs} - \sqrt{\frac{35}{6}}\mu_e\right)\right]\\
&\quad\times(-i)^{2m_l-\Delta m_F+2}e^{-b^2/w_0^2}\left[e^{i(m_l+1-\Delta m_F)\phi_b}d^1_{\Delta m_F 1}(\theta_k)J_{m_l+1-\Delta m_F}(\varkappa b) - e^{i(m_l-1-\Delta m_F)\phi_b}d^1_{\Delta m_F-1}(\theta_k)J_{m_l-1-\Delta m_F}(\varkappa b)\right], \quad (5c)\\
&\langle F=1|E_I^V|F=2;\text{up}\rangle\\
&= (-1)^{m_{F_i}}\mathcal{E}_0\begin{pmatrix}2 & 1 & 1\\ m_{F_i} & \Delta m_F & -m_{F_f}\end{pmatrix}\left[\sqrt{1-c_m^2}\left(\frac{\sqrt{15}}{2}\mu_e - \frac{\sqrt{5}}{2\sqrt{3}}\mu_{is}\right) + c_m\sqrt{2\pi}\sqrt{B(M1)}\right]\\
&\quad\times(-i)^{2m_l-\Delta m_F+2}e^{-b^2/w_0^2}\left[e^{i(m_l+1-\Delta m_F)\phi_b}d^1_{\Delta m_F 1}(\theta_k)J_{m_l+1-\Delta m_F}(\varkappa b) - e^{i(m_l-1-\Delta m_F)\phi_b}d^1_{\Delta m_F-1}(\theta_k)J_{m_l-1-\Delta m_F}(\varkappa b)\right], \quad (5d)\\
&\langle F=2;\text{up}|E_I^V|F=2;\text{down}\rangle\\
&= (-1)^{m_{F_i}}\mathcal{E}_0\left[\frac{\sqrt{2\pi}(2c_m^2-1)}{3}\sqrt{B(M1)} + c_m\sqrt{1-c_m^2}\left(\frac{5\sqrt{15}}{6}\mu_e + \frac{\sqrt{15}}{2}\mu_{is} - \frac{7}{\sqrt{15}}\mu_{gs}\right)\right]\\
&\quad\times(-i)^{2m_l-\Delta m_F}e^{-b^2/w_0^2}\begin{pmatrix}2 & 1 & 2\\ m_{F_i} & \Delta m_F & -m_{F_f}\end{pmatrix}\left[e^{i(m_l+1-\Delta m_F)\phi_b}d^1_{\Delta m_F 1}(\theta_k)J_{m_l+1-\Delta m_F}(\varkappa b)\right.\\
&\quad\left. - e^{i(m_l-1-\Delta m_F)\phi_b}d^1_{\Delta m_F-1}(\theta_k)J_{m_l-1-\Delta m_F}(\varkappa b)\right]. \quad (5e)
\end{aligned}$$

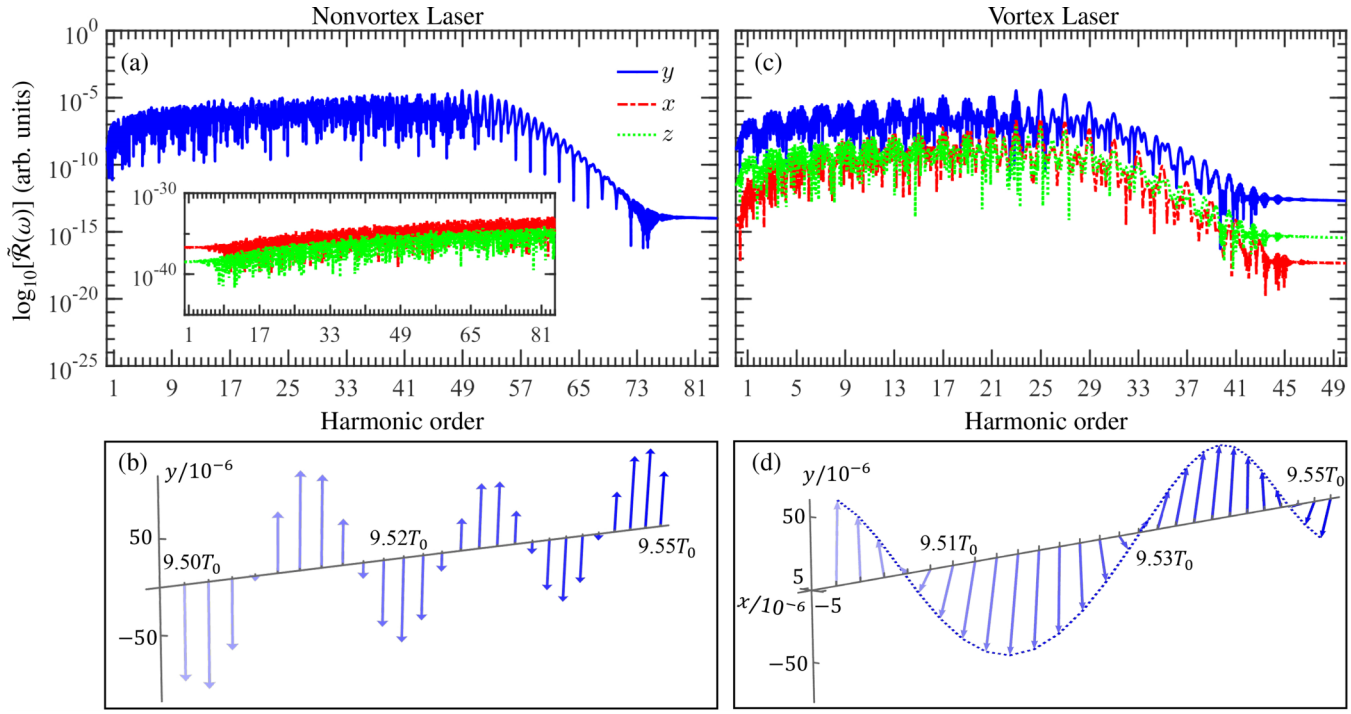


FIG. 2. (a) Radiation spectrum of the nonvortex laser-driven $^{229}Th^{89+}$ system, with laser wavelength of $\lambda_0 = 800$ nm, peak intensity of $I_0 = 10^{22}$ W/cm$^2$, pulse duration of $\tau = 20T_0$ ($T_0 = 2.67$ fs as the optical period), and temporal envelope $\sin^2(\pi t/\tau)$. Line styles represent the contributions from $\tilde{\mathcal{R}}_x$, $\tilde{\mathcal{R}}_y$, and $\tilde{\mathcal{R}}_z$. The horizontal axis is in units of laser photon energy (1.55 eV). (b) Time evolution of the reconstructed $\langle \mathbf{a} \rangle$ (atomic units) between $9.5T_0$ and $9.55T_0$, with arrow color deepening to indicate time passage; arrows are spaced by $0.002T_0$. (c) and (d) Similar to (a) and (b), but for a vortex laser. Parameters: OAM projection $m_l = 1$, pitch angle $\theta_k = 5^\circ$, beam waist $w_0 = 10\lambda_0$, impact parameter $\varkappa b = 2$, and $\phi_b = 0^\circ$.

Here, $\mathcal{E}_0$, $\mu_e$, $J_n(z)$, and $d^1_{\Delta m_F \pm 1}(\theta_k)$ represent laser electric field strength, the magnetic dipole moments of electron [31], the Bessel functions, and Wigner $d$ function at pitch angle $\theta_k = \varkappa/k_z$, respectively. $m_{F_i}$ ($m_{F_f}$) is the magnetic quantum number of the initial (final) state. $\mu_{\rm gs}$ and $\mu_{\rm is}$ denote the nuclear magnetic dipole moments of ground state and isomer state, with experimental values of 0.360 $\mu_N$ [69] and $-0.376$ $\mu_N$ [70], where $\mu_N$ is the nuclear magneton. $B(M1)$ is the reduced magnetic dipole transition probability, with the value 0.022 W.u. [9] adopted from experiment. Electric quadrupole contributions are negligible compared to the dominant magnetic dipole terms. The light-nucleus interaction displays two distinct features due to vortex effects. First, the impact parameter $\mathbf{b}$ provides an additional handle on state populations via the Bessel-Gauss profile $e^{-b^2/w_0^2} J_{m_l}(\varkappa b)$ and the azimuthal phase factor $e^{im_l\phi_b}$. Second, the transition selections are modified, allowing $\Delta m_F$ to take arbitrary values ($0, \pm 1$ for $M1$ transition) when $b \neq 0$.

By solving the time-dependent Schrödinger equation, we obtain the population of each state at every time step during the laser pulse. The radiation source is the laser-induced magnetic dipole moment, $\mathbf{m}(t) = \langle \Psi(t)|\hat{\mathbf{m}}|\Psi(t)\rangle$. The magnetic dipole moment operator is $\hat{\mathbf{m}} \propto rY_{lm}$ [60], with $\hat{m}_z \propto rY_{10}$, $\hat{m}_x \propto \frac{1}{\sqrt{2}}(rY_{1-1} - rY_{11})$, and $\hat{m}_y \propto \frac{i}{\sqrt{2}}(rY_{1-1} + rY_{11})$. The far-field radiation is treated within classical electrodynamics. Given the spatial nonuniformity of the vortex field, we calculate radiation spectra for dipole axes along the $x$, $y$, and $z$ directions as $\tilde{\mathcal{R}}_{(x,y,z)}(\omega) \propto |\int dt\, \ddot{\mathbf{m}}(t) e^{i\omega t}|^2$, where $\ddot{\mathbf{m}}(t)$ is the second time derivative of $\mathbf{m}(t)$. The acceleration of the nuclear magnetic moment $\langle \mathbf{a} \rangle(t) \propto \ddot{\mathbf{m}}(t)$ [71] can be reconstructed from the logic diagram in Fig. 1(b). Different vortex modes (e.g., Bessel and Laguerre-Gaussian) [46,72] exhibit varying asymptotic behaviors away from the beam axis, but this does not alter the qualitative conclusions (see Appendix). Other polarization states of incident vortex beam are evaluated in Appendix.

## III. RESULTS

### A. Nuclear magnetic moment rotation

To directly compare the OAM effect, we also calculate the same polarization condition (LP in the $x$ direction) using a nonvortex laser with a uniform transverse distribution as in [28], for the Gaussian beam is discussed in the Appendix. As shown in Fig. 2(a), high-order harmonic radiation from $^{229}Th^{89+}$ ion induced by the nonvortex laser results from the dipole axis contribution in the $y$ direction. Based on the radiation spectrum, the theoretically reconstructed acceleration $\langle \mathbf{a} \rangle$ oscillates temporally along the laser's magnetic field direction, which is the $y$ axis [see Fig. 2(b)]. For the radiation spectrum of $^{229}Th^{89+}$ ion induced by LP vortex laser, contributions are observed not only along the dipole axis in the $y$ direction but also result in high-order harmonics in the $x$ and $z$ directions [see Fig. 2(c)]. The appearance of noninteger

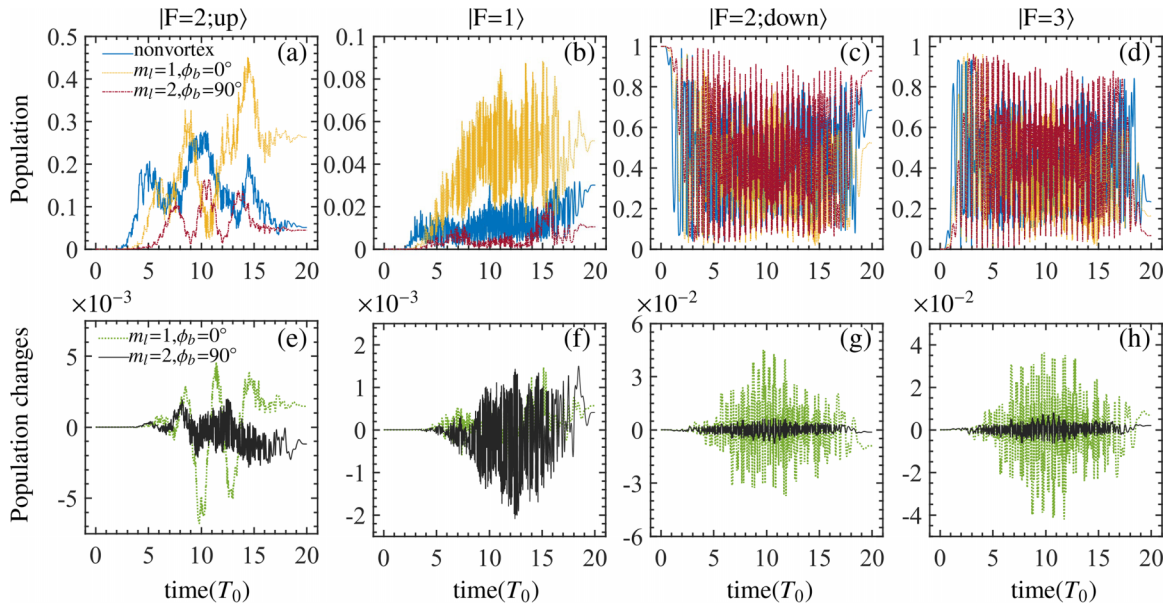


FIG. 3. (a)–(d) Time evolution of populations of $|F = 2; \text{up}\rangle$, $|F = 1\rangle$, $|F = 2; \text{down}\rangle$, and $|F = 3\rangle$ at $I_0 = 10^{22}$ W/cm$^2$ and $\tau = 20T_0$. Parameters for the vortex laser: $\theta_k = 5°$, $w_0 = 10\lambda_0$ and $\varkappa b = 2$. (e)–(h) Population changes resulting from manually switching off the $\Delta m_F = 0$ transitions.

harmonic orders arises from the extreme nonlinearity of the system. The reconstructed acceleration $\langle \mathbf{a} \rangle$ exhibits temporal rotation [see Fig. 2(d)], stemming from the reconfiguration of the system population by the vortex laser. The proposed method for reconstructing microscopic rotation exhibits robustness to relative random noise in the radiation spectrum under simulated experimental conditions. This stability arises from the crucial phase information [provided by theoretical calculation, see Fig. 1(b)], which encodes the essential rotational details and remains resilient to noise-induced amplitude fluctuations, thereby ensuring reliable reconstruction [73]. The two lowest-lying energy levels of the $^{229}$Th nucleus correspond to the band heads of two rotational bands. The rotation discussed here is that of the total magnetic moment arising from vortex-laser-driven superpositions of the system's wave function, and is distinct from nuclear vibrational and rotational excitations [74].

To elucidate why nuclear magnetic moment rotation occurs and why radiation signals differ significantly between nonvortex and vortex lasers (i.e., distinct $\tilde{\mathcal{R}}_x$ and $\tilde{\mathcal{R}}_z$), we calculate the time evolution of the system populations for both nonvortex and vortex laser cases and examine the population changes resulting from manually switching off the $\Delta m_F = 0$ transitions Fig. 3. When the light-nucleus interaction enters a highly nonlinear and nonperturbative regime, the reconfiguration of the system population in a vortex laser primarily stems from two factors. First, the primary factor affecting the system population arises from the localized electromagnetic field of the vortex laser, including the OAM and the introduction of an additional degree of control through the impact parameter **b**. These effects are also reflected in how the interaction matrix elements are influenced by the Bessel-Gauss beam flux $[e^{-b^2/w_0^2} J_{m_l}(\varkappa b)]$ and the azimuthal angle $e^{im_l\phi_b}$. Consequently, significant changes in the population dynamics Figs. 3(a)–3(d). Second, the transition selection rule is modified, and the channels $\Delta m_F = 0$ increase the diversity of energy states in excitation and de-excitation processes, resulting in a quantitative impact of approximately $10^{-2}$ to $10^{-3}$ on the time evolution of the population Figs. 3(e)–3(h). The influence of these new transition channels on the formation of microscopic rotation cannot be overlooked: when the new transition channels induced by the vortex laser are manually turned off, the radiation spectrum components $\tilde{\mathcal{R}}_x$ and $\tilde{\mathcal{R}}_z$ decrease by several orders of magnitude, causing the nuclear magnetic moment to dominate oscillations along the $y$ direction (see Appendix). Consequently, OAM of vortex laser reshapes the behavior of nuclear magnetic moments, transforming their motion from unidirectional oscillations to three-dimensional rotations. The extraction of the radiation spectrum offers a unique snapshot of microscopic rotation, yielding richer dynamic information about fundamental nuclear properties and structure, potentially improving measurement precision.

### B. Topologically protected periodic patterns

When the light-nucleus interaction deviates from the linear perturbative regime, we observe periodic patterns in the azimuthal angular dependence of nuclear radiation and excitation. The periodicity is determined by the OAM projection $m_l$ and exhibits topological protection as the laser intensity, pulse duration, and impact parameter vary. This represents a distinctive nonlinear signature of the nucleus induced by OAM. As the laser intensity decreases below the relativistic threshold, the light-nucleus interaction gradually returns to the linear perturbative regime, where the periodic patterns progressively disappear, consistent with previous studies [55,58].

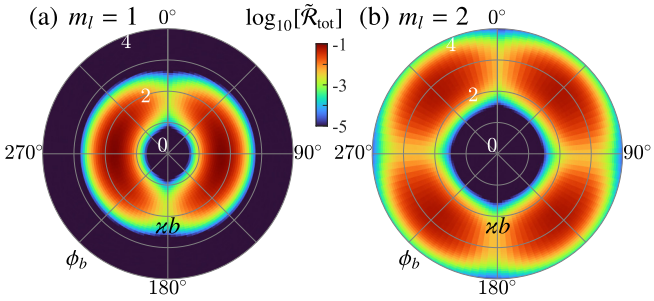


FIG. 4. (a) Distribution of radiation spectrum $\log_{10}[\tilde{\mathcal{R}}_{\rm tot}]$ on the impact parameter $\mathbf{b}$ for the vortex laser-driven $^{229}Th^{89+}$ system, where $\tilde{\mathcal{R}}_{\rm tot} = \tilde{\mathcal{R}}_x + \tilde{\mathcal{R}}_y + \tilde{\mathcal{R}}_z$. The radial component is $\varkappa b$, and the azimuthal component is $\phi_b$. Results correspond to the 27th harmonic order with laser parameters similar to those in Fig. 2(c). (b) Similar to (a), but for $m_l = 2$ and the 17th harmonic order.

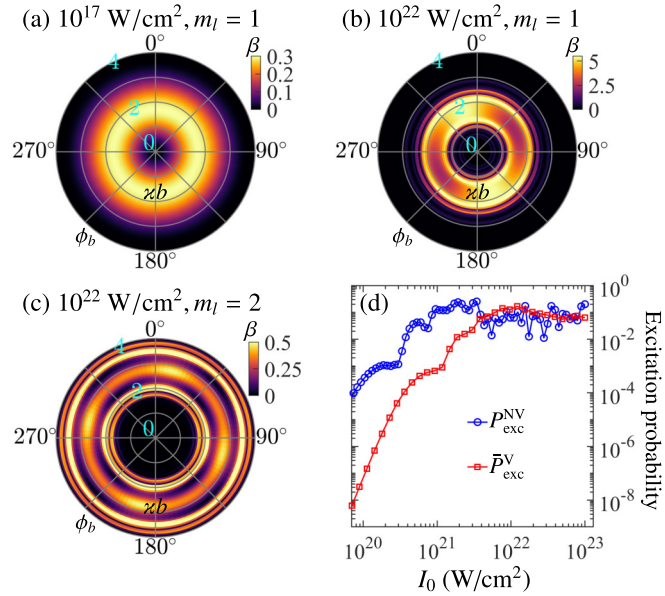


FIG. 5. Nuclear excitation probability of $^{229}Th^{89+}$ from the ground state to the isomeric state $|F = 2; \text{up}\rangle$ at the end of the laser pulse. (a)–(c) Distribution of excitation probability ratio ($\beta = P^{\rm V}_{\rm exc}/P^{\rm NV}_{\rm exc}$) between vortex and nonvortex lasers on the impact parameter $\mathbf{b}$ for various $I_0$ and $m_l$. (d) Excitation probability versus $I_0$ with pulse duration of $\tau = 10T_0$. The average excitation probability for the vortex laser, $\bar{P}^{\rm V}_{\rm exc}$, is calculated over $\mathbf{b} \leqslant \mathbf{b}_0$ as $\bar{P}^{\rm V}_{\rm exc} = \int_0^{\mathbf{b}_0} P^{\rm V}_{\rm exc}(\mathbf{b}) \frac{d^2\mathbf{b}}{\pi \mathbf{b}_0^2}$, where $|\mathbf{b}_0| = 3/\varkappa$. Other laser parameters match those in Fig. 2(c).

Figures 4(a) and 4(b) show the radiation spectra in the impact parameter $\mathbf{b}$ plane for $m_l = 1$ and $m_l = 2$, respectively. A periodic enhancement appears as a function of the azimuthal angle $\phi_b$, determined by the OAM projection $m_l$ and primarily arising from the contribution of $\tilde{\mathcal{R}}_y$. This phenomenon occurs in every harmonic order of the radiation spectrum, illustrated here with an example from the radiation platform region. Specifically, across the entire azimuthal angle, there are $2m_l$ radiation maxima and minima, with the radiation enhancement quantitatively increasing by several orders of magnitude. In contrast, the radiation in the nonvortex case is $\tilde{\mathcal{R}}_{\rm tot} \sim 10^{-5}$ [see Fig. 2(a)], comparable to the minima observed here, indicating that vortex laser substantially enhances the radiation from $^{229}Th^{89+}$ ion. Since periodic radiation enhancement arises from nonlinear effects induced by the topological charge of vortex laser when the strength of light-nucleus interaction deviates from the linear perturbative regime, the radiation pattern exhibits topological protection, where the azimuthal angles of the maxima and minima remain invariant regardless of the initial parameters ($I_0$, $\tau$, $b$), showing only quantitative variations in magnitude. As the laser intensity decreases into the perturbative regime, the enhancement magnitude diminishes and the periodic structure eventually disappears. Therefore, the use of vortex laser has the potential to significantly enhance high-order harmonic signals, thereby improving the precision of nuclear radiation measurements. Additionally, the spatial periodicity of radiation signals may serve as a spectroscopic method for extracting nuclear transition parameters [$B(M1)$, $\mu_{\rm is}$, $\mu_{\rm gs}$], while also providing experimental evidence of the nonlinear effects induced by OAM.

At relatively low intensities of $10^{17}$ W/cm$^2$, the excitation probabilities exhibit a linear relationship with the flux of vortex laser, consistent with the intuition that higher photon flux leads to increased excitation probabilities [see Fig. 5(a)]. In contrast to nonvortex laser, the effective peak intensity experienced by the $^{229}Th^{89+}$ ion is reduced when using vortex laser, resulting in suppressed excitation probabilities ($\beta < 1$). With further increases in laser peak intensity, such as $10^{22}$ W/cm$^2$ [see Fig. 5(b)], the light-nucleus interaction enters a highly nonlinear and nonperturbative regime. This is evidenced by the transformation of the radial impact parameter $b$ distribution from a single peak to a multi-peak structure, along with periodic variations in the azimuthal angle $\phi_b$. At the maxima, excitation probabilities may increase several times compared to the nonvortex laser case. The topological periodicity is determined by the OAM of vortex laser [see Figs. 5(b) and 5(c)], specifically $P^{\rm V}_{\rm exc}(\phi_b) = P^{\rm V}_{\rm exc}(\phi_b + 180^\circ/m_l)$, as the interaction energy $E^{\rm V}_{\rm I} \propto e^{im_l\phi_b}$. In the linear perturbative regime, the excitation probability $P^{\rm V}_{\rm exc} \propto |E^{\rm V}_{\rm I}|^2$ is independent of $\phi_b$. However, as laser intensity increases, nonlinear non-perturbative effects become significant, particularly in their dependence on $\phi_b$. Differing from the radiation spectrum (see Fig. 4), the maxima and minima of the excitation probability spectrum vary with changes in laser parameters ($I_0$, $\tau$) and impact parameters $b$. Because the excitation probability at the end of the laser pulse exhibits strong randomness, resulting from substantial temporal oscillations in the population of isomeric states. The probabilities of the upper level $|F = 1\rangle$ exhibit a similar pattern. In practice, we also consider the collision of the vortex laser with a target where ions are randomly distributed across the incident beam. For such a macroscopic target we average the excitation probability over the impact parameters $\mathbf{b} \leqslant \mathbf{b}_0$. As shown in Fig. 5(d), for the case of nonvortex laser, the excitation probability begins to saturate after the peak intensity reaches $10^{21}$ W/cm$^2$, subsequently entering a plateau oscillation region characterized by strong disorder and unpredictability. In contrast, for the vortex laser, saturation is delayed until approximately $10^{22}$ W/cm$^2$, and

the plateau region exhibits stability and predictability because averaging over the impact parameter **b** suppresses stochastic fluctuations.

### C. Experimental feasibility

Topological physics has been widely studied in fields such as condensed matter physics [75], quantum computing [76], photonics [77], and acoustics [78], primarily at atomic, molecular, and macroscopic scales. Here, we predict topological protection patterns at the nuclear scale, expanding conventional topological physics. These patterns manifest as distinct structures in excitation and radiation spectra across the **b** plane. Experimental validation relies on configurations such as ion storage rings [79,80] and Penning traps [81], which have reportedly integrated intense lasers or x-ray free-electron lasers [81–85]. However, experiments utilizing vortex lasers remain scarce but promising [86]. Current PW laser systems, including PHELIX at GSI [87] and SULF at SIOM [88], have already achieved vortex laser intensities in the range of $10^{18}$ to $10^{20}$ W/cm$^2$, and potentially even higher [49]. The vortex-laser wavelength, focal spot, and impact-parameter range used here match experimental studies [47,89]; the effects of ion's thermal position spread are evaluated in the Appendix. We propose potential experimental avenues: measuring the radiation spectrum of specific harmonic orders at different azimuthal angles centered around the vortex laser beam axis. Specifically, for a laser intensity of $10^{18}$ ($10^{20}$) W/cm$^2$, the third (fifth) harmonic exhibits a periodic enhancement by one order (two orders) of magnitude in the azimuthal radiation spectrum signal. With forthcoming 10–100 PW lasers [90,91], the analysis and reconstruction of radiation signals induced by stronger laser intensities should provide a snapshot of microrotation in nuclear magnetic moments.

## IV. CONCLUSION

In conclusion, through an examination of the interaction between intense vortex lasers and $^{229}$Th$^{89+}$ ions, our method could effectively excite and induce three-dimensional rotation of the nuclear magnetic moment on a femtosecond timescale, enabling unprecedented control over its behavior. Furthermore, introducing the OAM of vortex lasers into a chaotic system reveals topologically protected periodic patterns in nuclear excitation and radiation, serving as distinctive experimental signals. These findings suggest a valuable experimental probe for laser nuclear physics with vortex lasers, creating opportunities for high-precision nuclear control and imaging, and paving the way for innovative applications in fundamental physics, quantum information science, and advanced nuclear technologies, despite the challenges of thorium scarcity.


## ACKNOWLEDGMENTS

We thank M. F. Ciappina and B. K. Das for helpful discussions. The work is supported by the National Natural Science Foundation of China (Grants No. 12425510, No. U2267204, No. 12441506, No. 12447106, No. 123B2082, No. 12474484, No. U2330401, and No. 12088101), the National Key Research and Development (R&D) Program (Grant No. 2024YFA1610900), the Science Challenge Project (No. TZ2025012), and the Innovative Scientific Program of CNNC.


## DATA AVAILABILITY

The data that support the findings of this article are not publicly available. The data are available from the authors upon reasonable request.

## APPENDIX: ADDITIONAL DISCUSSION

*Benchmark*. We benchmarked the excitation Fig. 6(a) and radiation Fig. 6(b) of $^{229}$Th$^{89+}$ ions in the vortex limit and verified that these processes revert to the nonvortex scenario. We also evaluated how different vortex modes (e.g., Bessel, Bessel-Gauss, Laguerre-Gaussian) affect the interaction energies. Although their asymptotic behavior differs far from the beam axis, the qualitative conclusions remain unchanged Fig. 6(c).

*Vortex laser polarization*. For the various polarization states of incident vortex light, the vector potential of vortex light for LP in $y$ direction, radially polarized (RP) and azimuthally polarized (AP) can be written as [68]

$$\boldsymbol{A}^{\mathrm{V}}_{\mathrm{LP-y}} = \frac{1}{\sqrt{2}}\left(\boldsymbol{A}^{\mathrm{BG}}_{m_\gamma=m_l+1,\Lambda=1} + \boldsymbol{A}^{\mathrm{BG}}_{m_\gamma=m_l-1,\Lambda=-1}\right), \tag{6a}$$

$$\boldsymbol{A}^{\mathrm{V}}_{\mathrm{r}} = \frac{-i}{\sqrt{2}}\left(\boldsymbol{A}^{\mathrm{BG}}_{m_\gamma=0,\Lambda=1} + \boldsymbol{A}^{\mathrm{BG}}_{m_\gamma=0,\Lambda=-1}\right), \tag{6b}$$

$$\boldsymbol{A}^{\mathrm{V}}_{\mathrm{az}} = \frac{1}{\sqrt{2}}\left(\boldsymbol{A}^{\mathrm{BG}}_{m_\gamma=0,\Lambda=-1} - \boldsymbol{A}^{\mathrm{BG}}_{m_\gamma=0,\Lambda=1}\right). \tag{6c}$$

Consider the transition between $|F=2;\mathrm{down}\rangle$ and $|F=2;\mathrm{up}\rangle$ with the magnetic quantum numbers of the two states being $\{m_{\mathrm{down}}, m_{\mathrm{up}}\}$. The time-independent interaction matrix element for various polarization states, can be expressed as follows:

$$\begin{aligned}
&\langle F=2;\mathrm{up}|E^{\mathrm{V}}_{\mathrm{LP-y}}|F=2;\mathrm{down}\rangle \\
&= (-1)^{m_{F_i}}\mathcal{E}_0\left[\frac{\sqrt{2\pi}\left(2c_m^2-1\right)}{3}\sqrt{B(M1)} + c_m\sqrt{1-c_m^2}\left(\frac{5\sqrt{15}}{6}\mu_e + \frac{\sqrt{15}}{2}\mu_{\mathrm{is}} - \frac{7}{\sqrt{15}}\mu_{\mathrm{gs}}\right)\right]e^{-b^2/w_0^2} \\
&\times (-i)^{2m_l-\Delta m_F+1}\begin{pmatrix} 2 & 1 & 2 \\ m_{\mathrm{down}} & \Delta m_F & -m_{\mathrm{up}}\end{pmatrix}\left[e^{i(m_l+1-\Delta m_F)\phi_b}d^1_{\Delta m_F 1}(\theta_k)J_{m_l+1-\Delta m_F}(\varkappa b)\right. \\
&\left. + e^{i(m_l-1-\Delta m_F)\phi_b}d^1_{\Delta m_F-1}(\theta_k)J_{m_l-1-\Delta m_F}(\varkappa b)\right],
\end{aligned} \tag{7a}$$

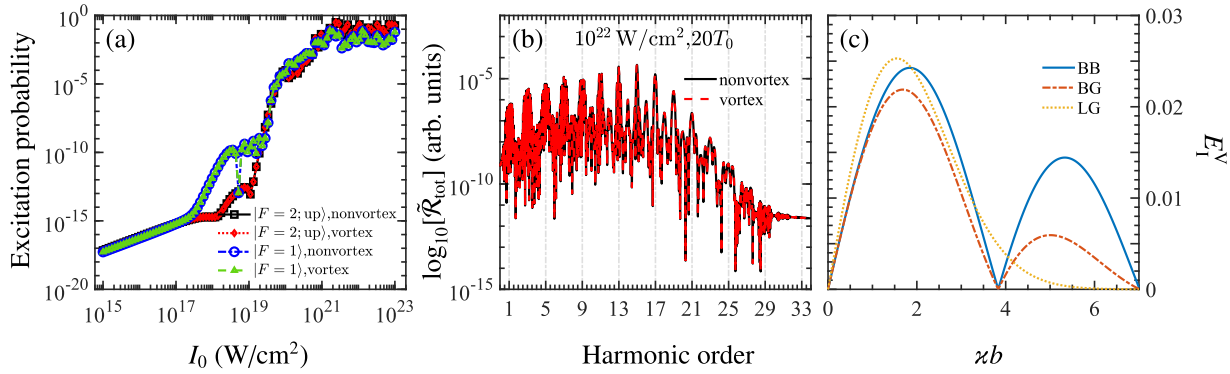


FIG. 6. (a) Excitation probabilities for $|F=2;\mathrm{up}\rangle$ and $|F=1\rangle$ versus laser intensity in nonvortex and vortex limits. The parameters for the "vortex limits case" are specified as $m_l=0$, $\theta_k=0.1^\circ$, $b=0$, and the pulse duration is $\tau=20T_0$. (b) Radiation spectra in nonvortex and vortex limits at peak intensity of $I_0=10^{22}$ W/cm$^2$. The horizontal axis is in units of laser photon energy (1.55 eV). (c) The amplitude of the interaction energies between $|F=2;\mathrm{down}\rangle$ and $|F=2;\mathrm{up}\rangle$ (with $m_{\mathrm{down}}=-2$ and $m_{\mathrm{up}}=-1$) for BB, BG, and LG beams versus $\varkappa b$. The pitch angle is $\theta_k=5^\circ$, the LG radial node is $p=0$ and the beam waist is $4\lambda_0$. Other parameters are similar to (b).

$$\begin{aligned}
&\langle F=2;\mathrm{up}|E_{\mathrm{r}}^{\mathrm{V}}|F=2;\mathrm{down}\rangle\\
&=(-1)^{m_{F_i}+1}\mathcal{E}_0\left[\frac{\sqrt{2\pi}\left(2c_m^2-1\right)}{3}\sqrt{B(M1)}+c_m\sqrt{1-c_m^2}\left(\frac{5\sqrt{15}}{6}\mu_e+\frac{\sqrt{15}}{2}\mu_{\mathrm{is}}-\frac{7}{\sqrt{15}}\mu_{\mathrm{gs}}\right)\right]\\
&\quad\times(-i)^{2m_l-\Delta m_F}e^{-b^2/w_0^2}\begin{pmatrix}2 & 1 & 2\\ m_{\mathrm{down}} & \Delta m_F & -m_{\mathrm{up}}\end{pmatrix}e^{-i\Delta m_F\phi_b}J_{-\Delta m_F}(\varkappa b)\left[d^1_{\Delta m_F 1}(\theta_k)+d^1_{\Delta m_F-1}(\theta_k)\right],
\end{aligned}\tag{7b}$$

$$\begin{aligned}
&\langle F=2;\mathrm{up}|E_{\mathrm{az}}^{\mathrm{V}}|F=2;\mathrm{down}\rangle\\
&=(-1)^{m_{F_i}+1}\mathcal{E}_0\left[\frac{\sqrt{2\pi}\left(2c_m^2-1\right)}{3}\sqrt{B(M1)}+c_m\sqrt{1-c_m^2}\left(\frac{5\sqrt{15}}{6}\mu_e+\frac{\sqrt{15}}{2}\mu_{\mathrm{is}}-\frac{7}{\sqrt{15}}\mu_{\mathrm{gs}}\right)\right]\\
&\quad\times(-i)^{2m_l-\Delta m_F+1}e^{-b^2/w_0^2}\begin{pmatrix}2 & 1 & 2\\ m_{\mathrm{down}} & \Delta m_F & -m_{\mathrm{up}}\end{pmatrix}e^{-i\Delta m_F\phi_b}J_{-\Delta m_F}(\varkappa b)\left[d^1_{\Delta m_F 1}(\theta_k)-d^1_{\Delta m_F-1}(\theta_k)\right].
\end{aligned}\tag{7c}$$

We have evaluated the effects of other polarization states Fig. 7. We find that for an LP vortex laser, regardless of whether the polarization is along the $x$ or $y$ axis, key results including rotation of the nuclear magnetic moment and the topological protection pattern in nuclear excitation and radiation remain unchanged. However, for RP and AP beams, which are superpositions of specific vortex states (i.e., linear combinations of two vortex beams with helicity $\Lambda=\pm1$ and OAM $m_l=\mp1$), the OAM is canceled by the helicity, leading to results similar to the non-vortex case. Specifically, as shown in Figs. 7(a1) and 7(a2), for the nonvortex laser (LP in the $y$ direction), high-order harmonic radiation from $^{229}\mathrm{Th}^{89+}$ ion results from the dipole axis contribution in the $x$ direction, and the reconstructed acceleration $\langle\mathbf{a}\rangle$ oscillates temporally along the laser's magnetic field direction ($x$ axis). In contrast, for the vortex laser under the same polarization condition, the multidimensional radiation signal corresponds to the temporal rotation of the reconstructed acceleration $\langle\mathbf{a}\rangle$ Figs. 7(b1) and 7(b2). Furthermore, the $\phi_b$ dependence of the radiation and absorption spectra shows a periodic structure, which disappears for RP and AP lasers Figs. 7(c) and 7(d).

*Gaussian beam*. We have evaluated the nonvortex case using a Gaussian beam. Our main conclusions hold for both plane waves and Gaussian beams. No topological protection pattern emerges in the nuclear excitation or radiation spectra with a Gaussian beam Fig. 8(a). However, a Gaussian beam, owing to its transverse intensity profile, the excitation probability exhibits impact parameter dependence, and shows nonlinear effects as peak intensity increases Fig. 8(b).

*Effects of new transition channels*. In the nonvortex case, where $\Delta m_F=0$ transitions are naturally absent, a strong suppression of the $x$ and $z$ components is already observed. For the vortex laser, when we manually block the $\Delta m_F=0$ transitions, we observe a similar trend: a suppression of the radiation spectrum components $\tilde{\mathcal{R}}_x$ and $\tilde{\mathcal{R}}_z$ by several orders of magnitude, causing the nuclear magnetic moment to dominate oscillations along the $y$ direction Fig. 9. This suppression stems from the relatively small changes in population discussed in Fig. 3. Therefore, the influence of these new transition channels on the formation of microscopic rotation cannot be overlooked. Here, we select the parameters $m_l=1,\phi_b=0^\circ$ and $m_l=2,\phi_b=90^\circ$ as examples, as these correspond to conditions where the effect of nuclear magnetic moment rotation is relatively pronounced. Since the $\tilde{\mathcal{R}}_y$ component exhibits periodic radiation enhancement in response

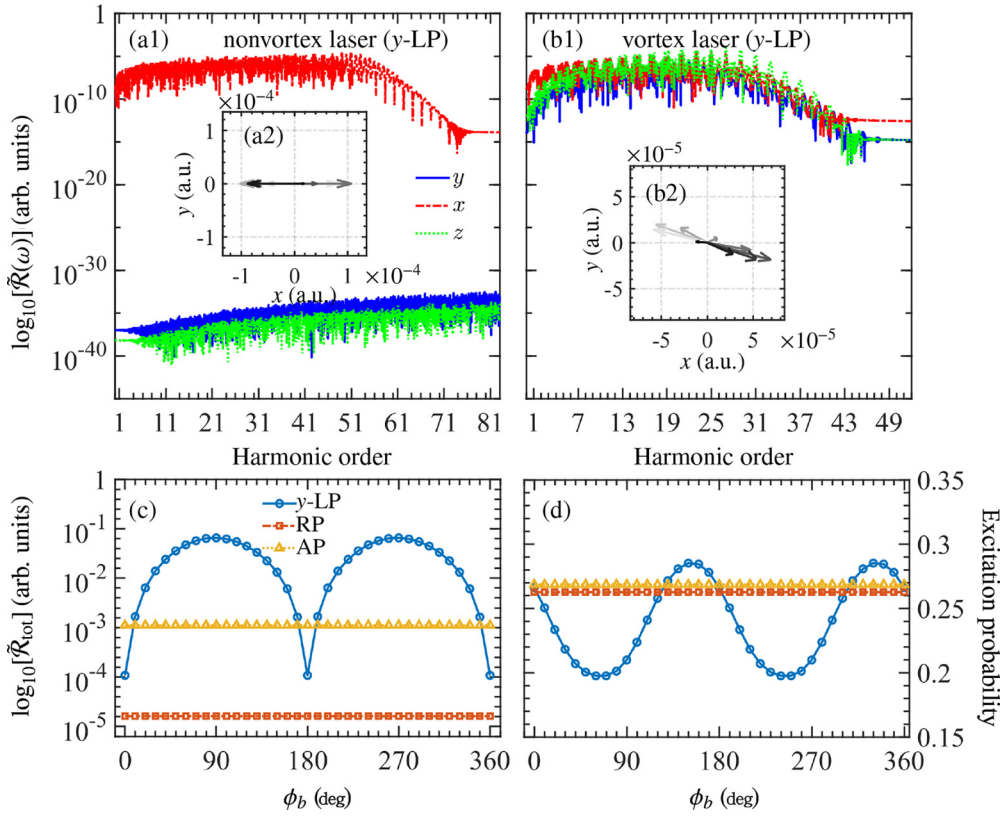


FIG. 7. (a1) Radiation spectrum of $^{229}Th^{89+}$ ion driven by a nonvortex laser (LP in $y$ direction) with $I_0 = 10^{22}$ W/cm$^2$ and $\tau = 20T_0$. Line styles represent the contributions from $\tilde{\mathcal{R}}_x$, $\tilde{\mathcal{R}}_y$, and $\tilde{\mathcal{R}}_z$. (a2) Time evolution of $\langle \mathbf{a} \rangle$ in $xy$ plane from $10.00T_0$ to $10.04T_0$; arrow color darkens with time. (b1), (b2) Same as (a1), (a2) but for a vortex laser with $m_l = 1$, $\theta_k = 5°$, $w_0 = 10\lambda_0$, $\varkappa b = 2$, and $\phi_b = 0°$. Radiation of the 27th harmonic (c) and excitation spectra (d) versus $\phi_b$, with other parameters as in (b1). Line styles correspond to various polarization states.

to the OAM, the magnitude of the nuclear magnetic moment rotation effect also displays periodicity.

*Effects of ion's thermal position spread.* In practice, it is necessary to consider the overlap between the beam's field profile and the ion's thermal position spread. For instance, in the experiment on the modification of transition selection rules with light OAM [47], the employed $^{40}Ca^+$ ion has a thermal position spread of approximately 60 nm. The scale of thermal position fluctuations can be estimated using a classical physics model given by $\langle x^2 \rangle \sim k_B T/k$, where $k_B$ is Boltzmann's constant, $T$ is the absolute temperature, and $k$ is the effective spring constant related to the shape and depth of the potential well that the ion occupies. For the highly charged thorium ion $^{229}Th^{89+}$, its larger mass yields a

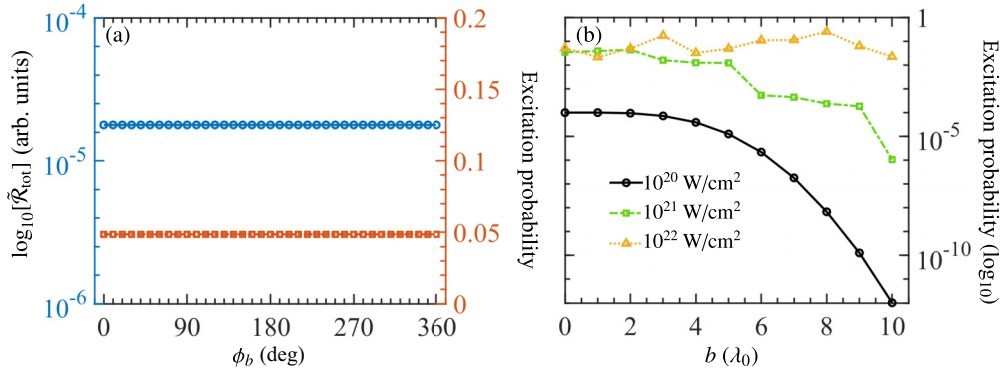


FIG. 8. Response of $^{229}Th^{89+}$ ion to a Gaussian laser pulse ($\tau = 20T_0$, $w_0 = 10\lambda_0$). (a) Radiation of the 37th harmonic (left axis) and excitation spectra (right axis) versus $\phi_b$ at peak intensity $I_0 = 10^{22}$W/cm$^2$ and impact parameter $b = 5\lambda_0$. (b) Excitation probability versus $b$ for various peak intensities at $\phi_b = 0°$.

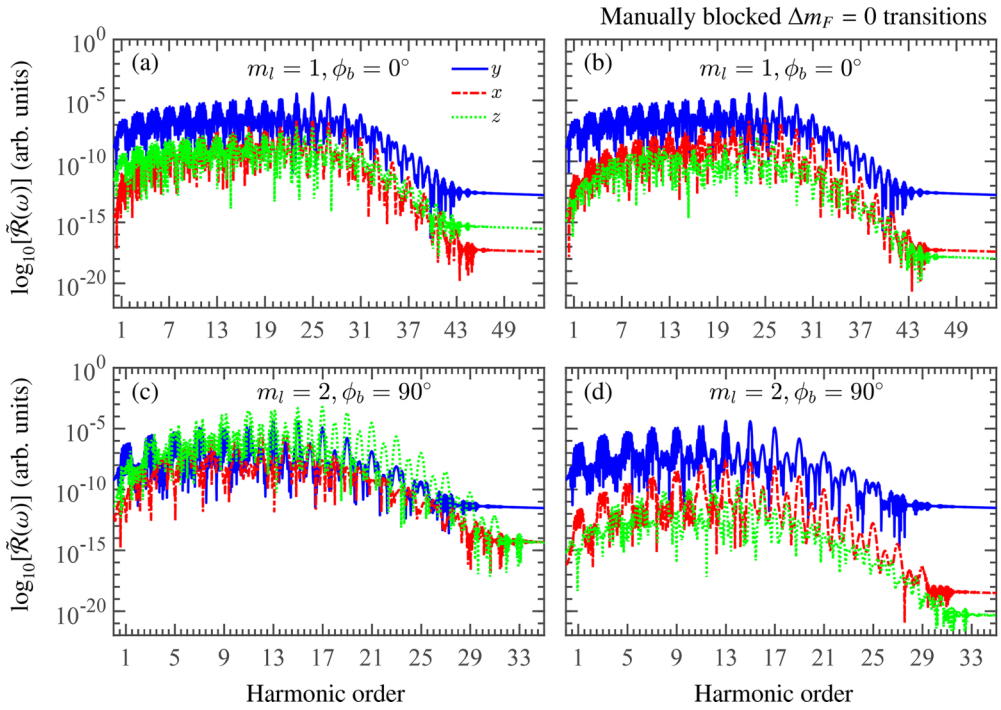


FIG. 9. (a) Radiation spectrum of the vortex laser-driven $^{229}Th^{89+}$ ion. Parameters: $I_0 = 10^{22}$ W/cm$^2$, $\tau = 20T_0$, $m_l = 1$, $\theta_k = 5°$, $w_0 = 10\lambda_0$, $\varkappa b = 2$ and $\phi_b = 0°$. Line styles represent contributions from $\tilde{\mathcal{R}}_x$, $\tilde{\mathcal{R}}_y$, and $\tilde{\mathcal{R}}_z$. (b) Same as (a), but with the $\Delta m_F = 0$ transition manually switched off. (c) and (d) Same as (a) and (b), but with $m_l = 2$ and $\phi_b = 90°$.

relatively high effective spring constant $k$, resulting in smaller thermal position fluctuations compared to the lighter $^{40}Ca^+$ ion, approximately on the order of 1–10 nm. The exact values may further depend on experimental conditions, such as temperature and potential electromagnetic field interference. We calculate and validate our theoretical findings (periodic radiation enhancement) in the presence of position uncertainties $\Delta b = 10$, 60 nm Fig. 10. Therefore, the nonlinear response of the nucleus induced by the OAM of vortex laser could be verified by measuring the radiation spectrum of specific harmonic orders at different azimuthal angles centered around the vortex laser beam axis. Specifically, for a laser intensity of $10^{18}$ ($10^{20}$) W/cm$^2$, the third (fifth) harmonic exhibits a periodic enhancement by one order (two orders) of magnitude in the azimuthal radiation spectrum signal.

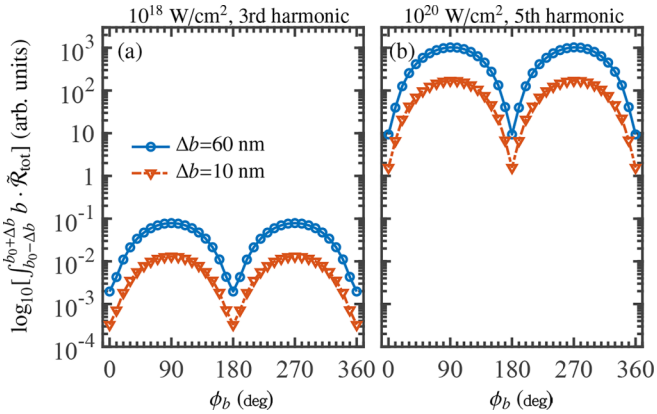


FIG. 10. (a) and (b) Radiation spectra of the vortex laser-driven $^{229}Th^{89+}$ ion as a function of $\phi_b$ for peak intensities of $10^{18}$ W/cm$^2$ and $10^{20}$ W/cm$^2$. The $y$ axis represents the integrated radiation intensity over the impact parameter, with $b_0 = 2/\varkappa$ ($\simeq 2.9$ μm). Circles and squares indicate integration ranges of $b_0 \pm 60$ nm and $b_0 \pm 10$ nm, respectively. Parameters: $\tau = 20T_0$, $m_l = 1$, $\theta_k = 5°$, and $w_0 = 10\lambda_0$.

[1] G. Fuchs, G. Burkard, P. Klimov, and D. Awschalom, A quantum memory intrinsic to single nitrogen–vacancy centres in diamond, Nat. Phys. **7**, 789 (2011).

[2] S. Zaiser, T. Rendler, I. Jakobi, T. Wolf, S.-Y. Lee, S. Wagner, V. Bergholm, T. Schulte-Herbrüggen, P. Neumann, and J. Wrachtrup, Enhancing quantum sensing sensitivity by a quantum memory, Nat. Commun. **7**, 12279 (2016).

[3] E. Andrew, A. Bradbury, and R. Eades, Nuclear magnetic resonance spectra from a crystal rotated at high speed, Nature (London) **182**, 1659 (1958).

[4] I. L. Pykett, J. H. Newhouse, F. S. Buonanno, T. J. Brady, M. R. Goldman, J. P. Kistler, and G. M. Pohost, Principles of nuclear magnetic resonance imaging, Radiology **143**, 157 (1982).

[5] J. B. Lambert, E. P. Mazzola, and C. D. Ridge, *Nuclear Magnetic Resonance Spectroscopy: An Introduction to Principles, Applications, and Experimental Methods* (John Wiley & Sons, New York, 2019).

[6] E. Coronado, Molecular magnetism: from chemical design to spin control in molecules, materials and devices, Nat. Rev. Mater. **5**, 87 (2020).

[7] X. Gao, S. Vaidya, K. Li, P. Ju, B. Jiang, Z. Xu, A. E. L. Allcca, K. Shen, T. Taniguchi, K. Watanabe, *et al.*, Nuclear spin polarization and control in hexagonal boron nitride, Nat. Mater. **21**, 1024 (2022).

[8] E. Peik and C. Tamm, Nuclear laser spectroscopy of the 3.5 eV transition in Th-229, Europhys. Lett. **61**, 181 (2003).

[9] J. Tiedau, M. Okhapkin, K. Zhang, J. Thielking, G. Zitzer, E. Peik, F. Schaden, T. Pronebner, I. Morawetz, L. T. De Col, F. Schneider, A. Leitner, M. Pressler, G. A. Kazakov, K. Beeks, T. Sikorsky, and T. Schumm, Laser excitation of the Th-229 nucleus, Phys. Rev. Lett. **132**, 182501 (2024).

[10] P. Walker and G. Dracoulis, Energy traps in atomic nuclei, Nature (London) **399**, 35 (1999).

[11] C. Chiara, J. Carroll, M. Carpenter, J. Greene, D. Hartley, R. Janssens, G. Lane, J. Marsh, D. Matters, M. Polasik, *et al.*, Isomer depletion as experimental evidence of nuclear excitation by electron capture, Nature (London) **554**, 216 (2018).

[12] G. C. Baldwin and J. C. Solem, Recoilless gamma-ray lasers, Rev. Mod. Phys. **69**, 1085 (1997).

[13] E. V. Tkalya, Proposal for a nuclear gamma-ray laser of optical range, Phys. Rev. Lett. **106**, 162501 (2011).

[14] A. Zilges, D. Balabanski, J. Isaak, and N. Pietralla, Photonuclear reactions—From basic research to applications, Prog. Part. Nucl. Phys. **122**, 103903 (2022).

[15] M. C. Downer, R. Zgadzaj, A. Debus, U. Schramm, and M. C. Kaluza, Diagnostics for plasma-based electron accelerators, Rev. Mod. Phys. **90**, 035002 (2018).

[16] D. Dubbers and M. G. Schmidt, The neutron and its role in cosmology and particle physics, Rev. Mod. Phys. **83**, 1111 (2011).

[17] V. Shiltsev and F. Zimmermann, Modern and future colliders, Rev. Mod. Phys. **93**, 015006 (2021).

[18] D. Balabanski, R. Popescu, D. Stutman, K. Tanaka, O. Tesileanu, C. Ur, D. Ursescu, and N. Zamfir, New light in nuclear physics: The extreme light infrastructure, Europhys. Lett. **117**, 28001 (2017).

[19] Z. Zhang, F. Wu, J. Hu, X. Yang, J. Gui, P. Ji, X. Liu, C. Wang, Y. Liu, X. Lu, *et al.*, The laser beamline in SULF facility, High Power Laser Sci. Eng. **8**, e4 (2020).

[20] J. W. Yoon, Y. G. Kim, I. W. Choi, J. H. Sung, H. W. Lee, S. K. Lee, and C. H. Nam, Realization of laser intensity over $10^{23}$ W/cm$^2$, Optica **8**, 630 (2021).

[21] J. Feng, W. Wang, C. Fu, L. Chen, J. Tan, Y. Li, J. Wang, Y. Li, G. Zhang, Y. Ma, *et al.*, Femtosecond pumping of nuclear isomeric states by the Coulomb collision of ions with quivering electrons, Phys. Rev. Lett. **128**, 052501 (2022).

[22] J. Feng, J. Qi, H. Zhang, S. Chen, M. Zhu, X. Hu, H. Xu, C. Fu, X. Wang, L. Chen, *et al.*, Laser-based approach to measure small nuclear cross sections in plasma, Proc. Natl. Acad. Sci. USA **121**, e2413221121 (2024).

[23] S. Gargiulo, I. Madan, B. Truc, P. Usai, K. Beeks, V. Leccese, G. M. Vanacore, and F. Carbone, Revisiting the excitation of the low-lying $^{181m}$Ta isomer in optical laser-generated plasma, Phys. Rev. Lett. **133**, 132501 (2024).

[24] R. E. Jacob, S. M. Tannous, L. A. Bernstein, J. Brown, T. Ostermayr, Q. Chen, D. H. G. Schneider, C. B. Schroeder, J. van Tilborg, E. H. Esarey, and C. G. R. Geddes, Enhanced isomer population via direct irradiation of solid-density targets using a compact laser-plasma accelerator, Phys. Rev. Lett. **134**, 052504 (2025).

[25] W. Wang, J. Zhou, B. Liu, and X. Wang, Exciting the isomeric $^{229}$Th nuclear state via laser-driven electron recollision, Phys. Rev. Lett. **127**, 052501 (2021).

[26] J. Qi, H. Zhang, and X. Wang, Isomeric excitation of $^{229}$Th in laser-heated clusters, Phys. Rev. Lett. **130**, 112501 (2023).

[27] W. Wang, F. Zou, S. Fritzsche, and Y. Li, Isomeric population transfer of the $^{229}$Th nucleus via hyperfine electronic bridge, Phys. Rev. Lett. **133**, 223001 (2024).

[28] H. Zhang, T. Li, and X. Wang, Highly nonlinear light-nucleus interaction, Phys. Rev. Lett. **133**, 152503 (2024).

[29] S. Wycech and J. Zylicz, Predictions for nuclear spin mixing in magnetic fields, Acta Phys. Pol. B **24**, 637 (1993).

[30] F. F. Karpeshin, S. Wycech, I. M. Band, M. B. Trzhaskovskaya, M. Pfützner, and J. Żylicz, Rates of transitions between the hyperfine-splitting components of the ground-state and the 3.5 eV isomer in $^{229}$Th$^{89+}$, Phys. Rev. C **57**, 3085 (1998).

[31] V. M. Shabaev, D. A. Glazov, A. M. Ryzhkov, C. Brandau, G. Plunien, W. Quint, A. M. Volchkova, and D. V. Zinenko, Ground-state $g$ factor of highly charged $^{229}$Th ions: An access to the M1 transition probability between the isomeric and ground nuclear states, Phys. Rev. Lett. **128**, 043001 (2022).

[32] W. Wang and X. Wang, Substantial nuclear hyperfine mixing effect in boronlike $^{205}$Pb ions, Phys. Rev. Lett. **133**, 032501 (2024).

[33] J. T. Lee, S. Alexander, S. Kevan, S. Roy, and B. McMorran, Laguerre–Gauss and Hermite–Gauss soft X-ray states generated using diffractive optics, Nat. Photon. **13**, 205 (2019).

[34] A. Luski, Y. Segev, R. David, O. Bitton, H. Nadler, A. R. Barnea, A. Gorlach, O. Cheshnovsky, I. Kaminer, and E. Narevicius, Vortex beams of atoms and molecules, Science **373**, 1105 (2021).

[35] C. W. Clark, R. Barankov, M. G. Huber, M. Arif, D. G. Cory, and D. A. Pushin, Controlling neutron orbital angular momentum, Nature (London) **525**, 504 (2015).

[36] B. J. McMorran, A. Agrawal, I. M. Anderson, A. A. Herzing, H. J. Lezec, J. J. McClelland, and J. Unguris, Electron vortex beams with high quanta of orbital angular momentum, Science **331**, 192 (2011).

[37] L. Allen, M. W. Beijersbergen, R. J. C. Spreeuw, and J. P. Woerdman, Orbital angular momentum of light and the transformation of Laguerre-Gaussian laser modes, Phys. Rev. A **45**, 8185 (1992).

[38] B. A. Knyazev and V. Serbo, Beams of photons with nonzero projections of orbital angular momenta: New results, Phys. Usp. **61**, 449 (2018).

[39] Y. Shen, X. Wang, Z. Xie, C. Min, X. Fu, Q. Liu, M. Gong, and X. Yuan, Optical vortices 30 years on: OAM manipulation from topological charge to multiple singularities, Light: Sci. Appl. **8**, 90 (2019).

[40] A. G. Peele, P. J. McMahon, D. Paterson, C. Q. Tran, A. P. Mancuso, K. A. Nugent, J. P. Hayes, E. Harvey, B. Lai, and I. McNulty, Observation of an x-ray vortex, Opt. Lett. **27**, 1752 (2002).

[41] B. Terhalle, A. Langner, B. Päivänranta, V. A. Guzenko, C. David, and Y. Ekinci, Generation of extreme ultraviolet vortex beams using computer generated holograms, Opt. Lett. **36**, 4143 (2011).

[42] G. Gariepy, J. Leach, K. T. Kim, T. J. Hammond, E. Frumker, R. W. Boyd, and P. B. Corkum, Creating high-harmonic beams with controlled orbital angular momentum, Phys. Rev. Lett. **113**, 153901 (2014).

[43] E. Hemsing, A. Knyazik, M. Dunning, D. Xiang, A. Marinelli, C. Hast, and J. B. Rosenzweig, Coherent optical vortices from relativistic electron beams, Nat. Phys. **9**, 549 (2013).

[44] I. P. Ivanov, Promises and challenges of high-energy vortex states collisions, Prog. Part. Nucl. Phys. **127**, 103987 (2022).

[45] R. Lange, N. Huntemann, A. A. Peshkov, A. Surzhykov, and E. Peik, Excitation of an electric octupole transition by twisted light, Phys. Rev. Lett. **129**, 253901 (2022).

[46] A. Afanasev, C. E. Carlson, C. T. Schmiegelow, J. Schulz, F. Schmidt-Kaler, and M. Solyanik, Experimental verification of position-dependent angular-momentum selection rules for absorption of twisted light by a bound electron, New J. Phys. **20**, 023032 (2018).

[47] C. T. Schmiegelow, J. Schulz, H. Kaufmann, T. Ruster, U. G. Poschinger, and F. Schmidt-Kaler, Transfer of optical orbital angular momentum to a bound electron, Nat. Commun. **7**, 12998 (2016).

[48] B. K. Das, C. Granados, M. Krüger, and M. F. Ciappina, High-order harmonic generation driven by perfect optical vortex beams: Exploring the orbital angular momentum upscaling law, Phys. Rev. Res. **6**, 043244 (2024).

[49] Y. Shi, X. Zhang, A. Arefiev, and B. Shen, Advances in laser-plasma interactions using intense vortex laser beams, Sci. China Phys. Mech. Astron. **67**, 295201 (2024).

[50] K. A. Forbes and D. L. Andrews, Optical orbital angular momentum: Twisted light and chirality, Opt. Lett. **43**, 435 (2018).

[51] F. Trawi, F. Billard, O. Faucher, P. Béjot, and E. Hertz, Molecular quantum interface for storing and manipulating ultrashort optical vortex, Laser Photon. Rev. **17**, 2200525 (2023).

[52] V. Garcés-Chávez, D. McGloin, M. J. Padgett, W. Dultz, H. Schmitzer, and K. Dholakia, Observation of the transfer of the local angular momentum density of a multiringed light beam to an optically trapped particle, Phys. Rev. Lett. **91**, 093602 (2003).

[53] G. A. Swartzlander Jr., E. L. Ford, R. S. Abdul-Malik, L. M. Close, M. A. Peters, D. M. Palacios, and D. W. Wilson, Astronomical demonstration of an optical vortex coronagraph, Opt. Express **16**, 10200 (2008).

[54] P. Kazinski and A. Sokolov, Excitation of multipolar transitions in nuclei by twisted photons, Phys. At. Nucl. **87**, 561 (2024).

[55] T. Kirschbaum, T. Schumm, and A. Pálffy, Photoexcitation of the $^{229}$Th nuclear clock transition using twisted light, Phys. Rev. C **110**, 064326 (2024).

[56] A. Afanasev and C. E. Carlson, Delta baryon photoproduction with twisted photons, Ann. Phys. (NY) **534**, 2100228 (2022).

[57] A. Afanasev, V. G. Serbo, and M. Solyanik, Radiative capture of cold neutrons by protons and deuteron photodisintegration with twisted beams, J. Phys. G: Nucl. Part. Phys. **45**, 055102 (2018).

[58] Z.-W. Lu, L. Guo, Z.-Z. Li, M. Ababekri, F.-Q. Chen, C. Fu, C. Lv, R. Xu, X. Kong, Y.-F. Niu, and J.-X. Li, Manipulation of giant multipole resonances via vortex $\gamma$ photons, Phys. Rev. Lett. **131**, 202502 (2023).

[59] Z.-W. Lu, L. Guo, M. Ababekri, J.-L. Zhang, X.-F. Weng, Y. Wu, Y.-F. Niu, and J.-X. Li, Angular momentum resolved inelastic electron scattering for nuclear giant resonances, Phys. Rev. Lett. **134**, 052501 (2025).

[60] J. M. Eisenberg and W. Greiner, *Nuclear Theory: Excitation Mechanisms of the Nucleus* (North-Holland Publishing Company, Amsterdam-London, 1976), Vol. 2.

[61] H. Zhang, T. Li, and X. Wang, Highly efficient nuclear excitation via highly nonlinear light-nucleus interaction, Phys. Rev. C **111**, 044614 (2025).

[62] L. von der Wense, P. V. Bilous, B. Seiferle, S. Stellmer, J. Weitenberg, P. G. Thirolf, A. Pálffy, and G. Kazakov, The theory of direct laser excitation of nuclear transitions, Eur. Phys. J. A **56**, 176 (2020).

[63] K. Alder, A. Bohr, T. Huus, B. Mottelson, and A. Winther, Study of nuclear structure by electromagnetic excitation with accelerated ions, Rev. Mod. Phys. **28**, 432 (1956).

[64] R. D. Cowan, *The Theory of Atomic Structure and Spectra*, Vol. 3 (University of California Press, Berkeley, 1981).

[65] J. H. Verner, Numerically optimal Runge–Kutta pairs with interpolants, Numer. Algor. **53**, 383 (2010).

[66] W. Wang and X. Wang, Quantum theory of isomeric excitation of $^{229}$Th in strong laser fields, Phys. Rev. Res. **5**, 043232 (2023).

[67] C. Sheppard and T. Wilson, Gaussian-beam theory of lenses with annular aperture, IEE J. Microw. Opt. Acoust. UK **2**, 105 (1978).

[68] S. A.-L. Schulz, A. A. Peshkov, R. A. Müller, R. Lange, N. Huntemann, C. Tamm, E. Peik, and A. Surzhykov, Generalized excitation of atomic multipole transitions by twisted light modes, Phys. Rev. A **102**, 012812 (2020).

[69] M. Safronova, U. Safronova, A. Radnaev, C. Campbell, and A. Kuzmich, Magnetic dipole and electric quadrupole moments of the $^{229}$Th nucleus, Phys. Rev. A **88**, 060501(R) (2013).

[70] J. Thielking, M. V. Okhapkin, P. Głowacki, D. M. Meier, L. von der Wense, B. Seiferle, C. E. Düllmann, P. G. Thirolf, and E. Peik, Laser spectroscopic characterization of the nuclear-clock isomer $^{229m}$Th, Nature (London) **556**, 321 (2018).

[71] W. Greiner, *Quantum Mechanics: An Introduction* (Springer Science & Business Media, Berlin, Heidelberg, 2011).

[72] J. Durnin, Exact solutions for nondiffracting beams. I. The scalar theory, J. Opt. Soc. Am. A **4**, 651 (1987).

[73] Z. Yuan, H. Wang, Z. Li, T. Wang, H. Wang, X. Huang, T. Li, Z. Ma, L. Zhu, W. Xu, *et al.*, Nuclear phase retrieval spectroscopy using resonant x-ray scattering, Nat. Commun. **16**, 3096 (2025).

[74] A. Bohr, Rotational motion in nuclei, Rev. Mod. Phys. **48**, 365 (1976).
[75] X.-L. Qi and S.-C. Zhang, Topological insulators and superconductors, Rev. Mod. Phys. **83**, 1057 (2011).
[76] B. Lian, X.-Q. Sun, A. Vaezi, X.-L. Qi, and S.-C. Zhang, Topological quantum computation based on chiral Majorana fermions, Proc. Natl. Acad. Sci. USA **115**, 10938 (2018).
[77] G.-J. Tang, X.-T. He, F.-L. Shi, J.-W. Liu, X.-D. Chen, and J.-W. Dong, Topological photonic crystals: physics, designs, and applications, Laser Photon. Rev. **16**, 2100300 (2022).
[78] H. Xue, Y. Yang, and B. Zhang, Topological acoustics, Nat. Rev. Mater. **7**, 974 (2022).
[79] M. Steck and Y. A. Litvinov, Heavy-ion storage rings and their use in precision experiments with highly charged ions, Prog. Part. Nucl. Phys. **115**, 103811 (2020).
[80] X. Ma, W. Wen, Z. Huang, H. Wang, Y. Yuan, M. Wang, Z. Sun, L. Mao, J. Yang, H. Xu, *et al.*, Proposal for precision determination of 7.8 eV isomeric state in $^{229}$Th at heavy ion storage ring, Phys. Scr. **T166**, 014012 (2015).
[81] S. Ringleb, M. Kiffer, N. Stallkamp, S. Kumar, J. Hofbrucker, B. Reich, B. Arndt, G. Brenner, M. Ruiz-Lopéz, S. Düsterer, *et al.*, High-intensity laser experiments with highly charged ions in a Penning trap, Phys. Scr. **97**, 084002 (2022).
[82] Z. Major, U. Eisenbarth, B. Zielbauer, C. Brabetz, J. Ohland, Y. Zobus, S. Roeder, D. Reemts, S. Kunzer, S. Götte, *et al.*, High-energy laser facility PHELIX at GSI: Latest advances and extended capabilities, High Power Laser Sci. Eng. **12**, e39 (2024).
[83] S. Kühn, C. Cheung, N. S. Oreshkina, R. Steinbrügge, M. Togawa, S. Bernitt, L. Berger, J. Buck, M. Hoesch, J. Seltmann, *et al.*, New measurement resolves key astrophysical Fe XVII oscillator strength problem, Phys. Rev. Lett. **129**, 245001 (2022).
[84] S. Sturm, I. Arapoglou, A. Egl, M. Höcker, S. Kraemer, T. Sailer, B. Tu, A. Weigel, R. Wolf, J. C. López-Urrutia, *et al.*, The ALPHATRAP experiment, Eur. Phys. J. Spec. Top. **227**, 1425 (2019).
[85] M. Horst, Z. Andelkovic, C. Brandau, R. J. Chen, D. Freire Fernández, C. Geppert, J. Glorius, V. Hannen, R. Heß, P. Imgram, *et al.*, Storage-ring laser spectroscopy of accelerator-produced hydrogen-like $^{208}$Bi$^{82+}$, Nat. Phys. **21**, 1057 (2025).
[86] F. An, D. Bai, S. Chen, X. Chen, H. Duyang, L. Gao, S.-F. Ge, J. He, J. Huang, Z. Huang, *et al.*, High-precision physics experiments at huizhou large-scale scientific facilities, Chin. Phys. Lett. **42**, 110102 (2025).
[87] C. Brabetz, S. Busold, T. Cowan, O. Deppert, D. Jahn, O. Kester, M. Roth, D. Schumacher, and V. Bagnoud, Laser-driven ion acceleration with hollow laser beams, Phys. Plasmas **22**, 013105 (2015).
[88] W. P. Wang, C. Jiang, H. Dong, X. M. Lu, J. F. Li, R. J. Xu, Y. J. Sun, L. H. Yu, Z. Guo, X. Y. Liang, Y. X. Leng, R. X. Li, and Z. Z. Xu, Hollow plasma acceleration driven by a relativistic reflected hollow laser, Phys. Rev. Lett. **125**, 034801 (2020).
[89] J.-L. Bégin, E. Karimi, P. Corkum, T. Brabec, and R. Bhardwaj, Orbital angular momentum control of strong-field ionization in atoms and molecules, Nat. Commun. **16**, 2467 (2025).
[90] C. Radier, O. Chalus, M. Charbonneau, S. Thambirajah, G. Deschamps, S. David, J. Barbe, E. Etter, G. Matras, S. Ricaud, *et al.*, 10 PW peak power femtosecond laser pulses at ELI-NP, High Power Laser Sci. Eng. **10**, e21 (2022).
[91] X. Wang, X. Liu, X. Lu, J. Chen, Y. Long, W. Li, H. Chen, X. Chen, P. Bai, Y. Li, *et al.*, 13.4 fs, 0.1 Hz OPCPA front end for the 100 PW-class laser facility, Ultrafast Sci. **2022**, 9894358 (2022).